J|A|C|S ARTICLES

Published on Web 10/26/2010

Electronic Modification of the $[Ru^{II}(tpy)(bpy)(OH_2)]^{2+}$ Scaffold: Effects on Catalytic Water Oxidation

Derek J. Wasylenko, Chelladurai Ganesamoorthy, Matthew A. Henderson, Bryan D. Koivisto, Hans D. Osthoff, and Curtis P. Berlinguette*

Department of Chemistry and Institute for Sustainable Energy, Environment & Economy, University of Calgary, 2500 University Drive N.W., Calgary, Canada T2N-1N4

Received July 9, 2010; E-mail: cberling@ucalgary.ca

Abstract: The mechanistic details of the Ce(IV)-driven oxidation of water mediated by a series of structurally related catalysts formulated as $[Ru(tpy)(L)(OH_2)]^{2+}$ [L = 2,2′-bipyridine (bpy), **1**; 4,4′-dimethoxy-2,2′-bipyridine (bpy-OMe), **2**; 4,4′-dicarboxy-2,2′-bipyridine (bpy-CO_2H), **3**; tpy = 2,2′;6″,2″-terpyridine] is reported. Cyclic voltammetry shows that each of these complexes undergo three successive (proton-coupled) electron-transfer reactions to generate the $[Ru^{V}(tpy)(L)O]^{3+}$ ($[Ru^{V}{=}O]^{3+}$) motif; the relative positions of each of these redox couples reflects the nature of the electron-donating or withdrawing character of the substituents on the bpy ligands. The first two (proton-coupled) electron-transfer reaction steps (k_1 and k_2) were determined by stopped-flow spectroscopic techniques to be faster for **3** than **1** and **2**. The addition of one (or more) equivalents of the terminal electron-acceptor, $(NH_4)_2[Ce(NO_3)_6]$ (CAN), to the $[Ru^{IV}(tpy)(L)O]^{2+}$ ($[Ru^{IV}{=}O]^{2+}$) forms of each of the catalysts, however, leads to divergent reaction pathways. The addition of 1 eq of CAN to the $[Ru^{IV}{=}O]^{2+}$ form of **2** generates $[Ru^{V}{=}O]^{3+}$ ($k_3 = 3.7\ M^{-1}\ s^{-1}$), which, in turn, undergoes slow O−O bond formation with the substrate ($k_{O-O} = 3 \times 10^{-5}\ s^{-1}$). The minimal (or negligible) thermodynamic driving force for the reaction between the $[Ru^{IV}{=}O]^{2+}$ form of **1** or **3** and 1 eq of CAN results in slow reactivity, but the rate-determining step is assigned as the liberation of dioxygen from the $[Ru^{IV}{-}OO]^{2+}$ level under catalytic conditions for each complex. Complex **2**, however, passes through the $[Ru^{V}{-}OO]^{3+}$ level prior to the rapid loss of dioxygen. Evidence for a competing reaction pathway is provided for **3**, where the $[Ru^{V}{=}O]^{3+}$ and $[Ru^{III}{-}OH]^{2+}$ redox levels can be generated by disproportionation of the $[Ru^{IV}{=}O]^{2+}$ form of the catalyst ($k_d = 1.2\ M^{-1}\ s^{-1}$). An auxiliary reaction pathway involving the abstraction of an O-atom from CAN is also implicated during catalysis. The variability of reactivity for **1**-**3**, including the position of the RDS and potential for O-atom transfer from the terminal oxidant, is confirmed to be intimately sensitive to electron density at the metal site through extensive kinetic and isotopic labeling experiments. This study outlines the need to strike a balance between the reactivity of the $[Ru{=}O]^{z}$ unit and the accessibility of higher redox levels in pursuit of robust and reactive water oxidation catalysts.

Introduction

The conversion of solar energy to chemical energy is a promising sustainable option for high-density energy storage and transportation.[1−5] In this context, there is a long-standing effort to develop molecular (photo)electrocatalysts to negotiate the proton-coupled electron-transfer (PCET) and thermodynamic ($E° = 1.23$ V at pH = 0) demands of extracting H_2 and O_2 fuels from water.[2,6−8] Drawing inspiration from the fact that the oxygen-evolving complex (OEC), the site of biological water oxidation catalysis within photosystem II, has been identified as a Mn_4O_4 cluster,[9−12] the majority of synthetic water oxidation catalysts have been designed to contain multiple metal centers.[6,13] The first reported synthetic water oxidation catalyst was the "blue dimer", *cis*,*cis*-$[(bpy)_2(H_2O)Ru^{III}ORu^{III}(OH_2)(bpy)_2]^{4+}$ (**I**; bpy = 2,2′-bipyridine).[14] Since that discovery almost three decades ago, a relatively small sample of compounds has demonstrated competence in mediating dioxygen formation from water. This list includes derivatives of the "blue dimer",[15]

(1) Nocera, D. G. *ChemSusChem* **2009**, *2*, 387–390.
(2) Eisenberg, R.; Nocera, D. G. *Inorg. Chem.* **2005**, *44*, 6799–6801 and references therein.
(3) Lewis, N. S.; Nocera, D. G. *Proc. Natl. Acad. Sci. U.S.A.* **2006**, *103*, 15729–15735.
(4) Armaroli, N.; Balzani, V. *Angew. Chem., Int. Ed.* **2006**, *46*, 52–66.
(5) Lewis, N. S. *Science* **2007**, *315*, 798–801.
(6) Eisenberg, R.; Gray, H. B. *Inorg. Chem.* **2008**, *47*, 1697–1699 and references therein.
(7) Huynh, M. H. V.; Meyer, T. J. *Chem. Rev.* **2007**, *107*, 5004–5064.
(8) Chang, C. J.; Chang, M. C. Y.; Damrauer, N. H.; Nocera, D. G. *Biochim. Biophys. Acta* **2004**, *1655*, 13–28.
(9) Ferreira, K. N.; Iverson, T. M.; Maghlaoui, K.; Barber, J.; Iwata, S. *Science* **2004**, *303*, 1831–1838.
(10) Stull, J. A.; Stich, T. A.; Service, R. J.; Debus, R. J.; Mandal, S. K.; Armstrong, W. H.; Britt, R. D. *J. Am. Chem. Soc.* **2010**, *132*, 446–447.
(11) Loll, B.; Kern, J.; Saenger, W.; Zouni, A.; Biesiadka, J. *Nature* **2005**, *438*, 1040–1044.
(12) Yano, J.; Kern, J.; Sauer, K.; Latimer, M. J.; Pushkar, Y.; Biesiadka, J.; Loll, B.; Saenger, W.; Messinger, J.; Zouni, A.; Yachandra, V. K. *Science* **2006**, *314*, 821–825.
(13) Yagi, M.; Kaneko, M. *Chem. Rev.* **2001**, *101*, 21–35.
(14) Gersten, S. W.; Samuels, G. J.; Meyer, T. J. *J. Am. Chem. Soc.* **1982**, *104*, 4029–4030.
(15) Rotzinger, F. P.; Munavalli, S.; Comte, P.; Hurst, J. K.; Grätzel, M.; Pern, F. J.; Frank, A. J. *J. Am. Chem. Soc.* **1987**, *109*, 6619–6626.

10.1021/ja106108y

bimetallic complexes of different geometries containing Ru and Mn active sites,[16−21] and polyoxometallic complexes containing Ru or Co.[22−24]

The landscape of homogeneous water oxidation catalysis has changed substantially in light of the recent discoveries that single-site complexes are capable of facilitating dioxygen formation from water.[25] The rapidly growing catalogue of mononuclear water oxidation catalysts now includes a family of cyclometalated Ir complexes reported by Bernhard et al.,[26] and a cyclopentadienyl Ir derivative documented by Crabtree and Brudvig.[27] There is also an extensive suite of polypyridyl Ru catalysts that have been independently reported by the research programs headed by Thummel,[17,28] Meyer,[25,29−31] Sun[32] and Sakai.[33] A related set of complexes have also served as useful platforms for *reducing* water directly to dihydrogen,[34] *oxidizing* water with the assistance of light,[24,35,36] and unraveling the intricate reaction details with theory.[37]

Despite these significant breakthroughs, there remains interest in gaining a precise understanding of the mechanistic details of water oxidation to further the collective pursuit of highly active catalysts that are not susceptible to deactivation. While there has been a wealth of knowledge gained by the extensive mechanistic and/or computational studies on **I**[14,38−40] (and related compounds[15]), the completely inorganic Ru-substituted polytungstate cluster $[\{Ru_4O_4(OH)_2(H_2O)_4\}(\gamma\text{-}SiW_{10}O_{36})_2]^{10-}$ (**II**),[22,23,41,42] the dimeric complexes $\{[Ru(tpy)(OH_2)]_2(\mu\text{-bpp})\}^{3+}$ (**III**; bpp = *bis*(2-pyridyl)-3,5-pyrazolate)[43] and $[(tpy)(OH_2)Mn^{III}(O)_2Mn^{IV}(OH_2)(tpy)]^{3+}$ (tpy = 2,2′;6′,2″-terpyridine),[44] and others,[13] there remain many advantages to the study of single-site Ru(II) complexes; e.g., synthetic accessibility; relatively well-defined spectroscopic and electrochemical properties for *in situ* studies; lower susceptibility to annation and lower computational time required for modeling studies.[29,37,45] Meyer et al. have taken advantage of these attributes to quantitatively describe a catalytic pathway negotiated by $[Ru^{II}(tpy)(bpm)(OH_2)]^{2+}$ (**IV**; bpm = 2,2′-bipyrimidine), $[Ru^{II}(tpy)(bpz)(OH_2)]^{2+}$ (**V**; bpz = 2,2′-pipyrazine), and related compounds.[25,29,31,46] The importance of this elegant work lies in the fact that it is one of the most well-defined pathways determined for a homogeneous water oxidation catalyst to date. A particularly compelling outcome of this analysis is the possibility that two catalytic pathways (i.e., Ru(II)/Ru(V) vs Ru(III)/Ru(V)) are operative depending on the conditions employed. Expanding on these studies, they have also provided experimental evidence to explain in explicit detail the critical O−O bond formation process.[47]

Building on these collective observations, our group is expanding the development of the water oxidation catalyst, $[Ru^{II}(tpy)(bpy)(OH_2)]^{2+}$ (**1**), to unravel the myriad catalytic pathways that may be possible during the oxidation of water.[48] We consider this complex, which was first reported to be a water oxidation catalyst in convincing fashion by Sakai et al.,[33] to have broad utility for furthering the development of homogeneous water oxidation catalysts because of the inherent tunability, stability in solution, and well-defined electrochemical and spectroscopic handles. By installing electron-donating and -withdrawing groups about the periphery of the polypyridyl ligands, for example, we have been able to directly correlate how catalytic activity and catalyst deactivation are affected by electron density at the metal.[48]

In this work, we further evaluate the mechanistic details associated with water splitting using a suite of Ru catalysts with electron-donating and -withdrawing substituents at the activating positions of the scaffold $[Ru^{II}(tpy)(bpy\text{-}R)(OH_2)]^{2+}$ [R = −H (**1**); −OMe (**2**); and $-CO_2H$ (**3**); bpy-OMe = 4,4′-dimethoxy-2,2′-bipyridine; bpy-CO_2H = 4,4′-dicarboxy-2,2′-bipyridine; Figure 1]. (Notation used in this article to describe redox and protonation levels: $[Ru^{II}—OH_2]^{2+} = [Ru^{II}(tpy)(bpy\text{-}R)(OH_2)]^{2+}$; $[Ru^{III}—OH_2]^{3+} = [Ru^{III}(tpy)(bpy\text{-}R)(OH_2)]^{3+}$; $[Ru^{IV}═O]^{2+}$ =

(16) Limburg, J.; Vrettos, J. S.; Liable-Sands, L. M.; Rheingold, A. L.; Crabtree, R. H.; Brudvig, G. W. *Science* **1999**, *283*, 1524–1527.
(17) Zong, R.; Thummel, R. *J. Am. Chem. Soc.* **2005**, *127*, 12802–12803.
(18) Muckerman, J. T.; Polyansky, D. E.; Wada, T.; Tanaka, K.; Fujita, E. *Inorg. Chem.* **2008**, *47*, 1787–1802.
(19) Wada, T.; Tsuge, K.; Tanaka, K. *Angew. Chem., Int. Ed.* **2000**, *39*, 1479–1482.
(20) Sens, C.; Romero, I.; Rodriguez, M.; Llobet, A.; Parella, T.; Benet-Buchholz, J. *J. Am. Chem. Soc.* **2004**, *126*, 7798–7799.
(21) Deng, Z. P.; Tseng, H. W.; Zong, R. F.; Wang, D.; Thummel, R. *Inorg. Chem.* **2008**, *47*, 1835–1848.
(22) Geletii, Y. V.; Botar, B.; Kögerler, P.; Hillesheim, D. A.; Musaev, D. G.; Hill, C. L. *Angew. Chem., Int. Ed.* **2008**, *47*, 3896–3899.
(23) Sartorel, A.; Carraro, M.; Scorrano, G.; De Zorzi, R.; Geremia, S.; McDaniel, N. D.; Bernhard, S.; Bonchio, M. *J. Am. Chem. Soc.* **2008**, *130*, 5006–5007.
(24) Yin, Q.; Tan, J. M.; Besson, C.; Geletii, Y. V.; Musaev, D. G.; Kuznetsov, A. E.; Luo, Z.; Hardcastle, K. I.; Hill, C. L. *Science* **2010**, *328*, 342–345.
(25) Concepcion, J. J.; Jurss, J. W.; Brennaman, M. K.; Hoertz, P. G.; Patrocinio, A. O. T.; Murakami Iha, N. Y.; Templeton, J. L.; Meyer, T. J. *Acc. Chem. Res.* **2009**, *42*, 1954–1965.
(26) McDaniel, N. D.; Coughlin, F. J.; Tinker, L. L.; Bernhard, S. *J. Am. Chem. Soc.* **2008**, *130*, 210–217.
(27) Hull, J. F.; Balcells, D.; Blakemore, J. D.; Incarvito, C. D.; Eisenstein, O.; Brudvig, G. W.; Crabtree, R. H. *J. Am. Chem. Soc.* **2009**, *131*, 8730–8731.
(28) Tseng, H.; Zong, R.; Muckerman, J. T.; Thummel, R. *Inorg. Chem.* **2008**, *47*, 11763–11773.
(29) Concepcion, J. J.; Tsai, M.-K.; Muckerman, J. T.; Meyer, T. J. *J. Am. Chem. Soc.* **2010**, *132*, 1545–1557.
(30) Concepcion, J. J.; Jurss, J. W.; Norris, M. R.; Chen, Z.; Templeton, J. L.; Meyer, T. J. *Inorg. Chem.* **2010**, *49*, 1277–1279.
(31) Concepcion, J. J.; Jurss, J. W.; Templeton, J. L.; Meyer, T. J. *J. Am. Chem. Soc.* **2008**, *130*, 16462–16463.
(32) Duan, L. L.; Fischer, A.; Xu, Y. H.; Sun, L. C. *J. Am. Chem. Soc.* **2009**, *131*, 10397–10399.
(33) Masaoka, S.; Sakai, K. *Chem. Lett.* **2009**, *38*, 182–183.
(34) Karunadasa, H. I.; Chang, C. J.; Long, J. R. *Nature* **2010**, *464*, 1329–1333.
(35) Duan, L.; Xu, Y.; Zhang, P.; Wang, M.; Sun, L. *Inorg. Chem.* **2010**, *49*, 209–215.
(36) Besson, C.; Huang, Z.; Geletii, Y. V.; Lense, S.; Hardcastle, K. I.; Musaev, D. G.; Lian, T.; Proust, A.; Hill, C. L. *Chem. Commun.* **2010**, *46*, 2784–2786.
(37) Wang, L.-P.; Wu, Q.; Van Voorhis, T. *Inorg. Chem.* **2010**, *49*, 4543–4553.
(38) Yang, X.; Baik, M.-H. *J. Am. Chem. Soc.* **2004**, *126*, 13222–13223.
(39) Yamada, H.; Siems, W. F.; Koike, T.; Hurst, J. K. *J. Am. Chem. Soc.* **2004**, *126*, 9786–9795.
(40) Binstead, R. A.; Chronister, C. W.; Ni, J.; Hartshorn, C. M.; Meyer, T. J. *J. Am. Chem. Soc.* **2000**, *122*, 8464–8473.
(41) Geletii, Y. V.; Huang, Z.; Hou, Y.; Musaev, D. G.; Lian, T.; Hill, C. L. *J. Am. Chem. Soc.* **2009**, *131*, 7522–7523.
(42) Sartorel, A.; Miro, P.; Salvadori, E.; Romain, S.; Carraro, M.; Scorrano, G.; Di Valentin, M.; Llobet, A.; Bo, C.; Bonchio, M. *J. Am. Chem. Soc.* **2009**, *131*, 16051–16053.
(43) Bozoglian, F.; Romain, S.; Ertem, M. Z.; Todorova, T. K.; Sens, C.; Mola, J.; Rodriguez, M.; Romero, I.; Benet-Buchholz, J.; Fontrodona, X.; Cramer, C. J.; Gagliardi, L.; Llobet, A. *J. Am. Chem. Soc.* **2009**, *131*, 15176–15187.
(44) Limburg, J.; Vrettos, J. S.; Chen, H.; de Paula, J. C.; Crabtree, R. H.; Brudvig, G. W. *J. Am. Chem. Soc.* **2001**, *123*, 423–430.
(45) Meyer, T. J.; Huynh, M. H. V. *Inorg. Chem.* **2003**, *42*, 8140–8160.
(46) Chen, Z.; Concepcion, J. J.; Jurss, J. W.; Meyer, T. J. *J. Am. Chem. Soc.* **2009**, *131*, 15580–15581.
(47) Chen, Z.; Concepcion, J. J.; Hu, X.; Yang, W.; Hoertz, P. G.; Meyer, T. J. *Proc. Natl. Acad. Sci. U.S.A.* **2010**, *107*, 7225–7229.
(48) Wasylenko, D. J.; Ganesamoorthy, C.; Koivisto, B. D.; Henderson, M. A.; Berlinguette, C. P. *Inorg. Chem.* **2010**, *49*, 2202–2209.

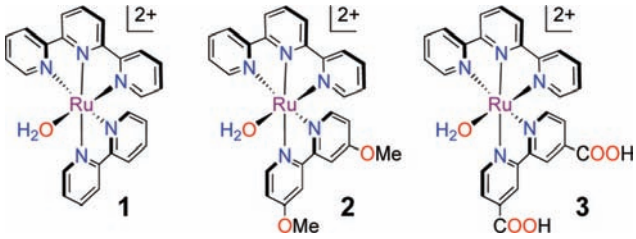

Figure 1. Compounds under investigation in this study (counterion = ClO_4^-).

$[Ru^{IV}(tpy)(bpy\text{-}R)O]^{2+}$; $[Ru^{V}{=}O]^{3+} = [Ru^{V}(tpy)(bpy\text{-}R)O]^{3+}$.) The location of the substituents on the pyridyl ligands was selected by virtue of our prior work, which showed that the catalytic behavior of derivatives of **1** is inherently more sensitive to substituents positioned on the bpy ligand rather than the tpy ligand because one of the pyridyl rings of the bpy ligand resides *trans* to the Ru−O bond.[48] The overarching goal of this study is to detail specifically how electronic density at the active site affects the catalytic performance while holding the balance of the structure at parity. While it is shown that each of the catalysts adhere in large part to the acid−base mechanism previously documented by Meyer et al., there are some distinctive differences in reactivity among the series that are highlighted by extensive kinetic and isotopic labeling experiments. This study offers clarity on how a balance must be established in terms of making the higher redox levels of the metal ion more accessible (e.g., by using an electron-rich ligand environment) and the reactivity of the [Ru=O] unit (e.g., electron deficient ligands). This work also outlines how an auxiliary reaction pathway involving the abstraction of an O-atom from a common terminal oxidant figures into the analysis of water oxidation catalysts.

Experimental Section

Preparation of Compounds. Ligands 2,2′;6′,2″-terpyridine (tpy), 4,4′-dimethoxy-2,2′-bipyridine (bpy-OMe), and 2,2′-bipyridine (bpy) and metal complex precursor $RuCl_3 \cdot 3H_2O$ were purchased from Aldrich and Pressure Chemical Company, respectively, and used without further purification. The ligand 4,4′-dicarboxy-2,2′-bipyridine (bpy-CO_2H) was synthesized according to a published procedure.[49] Compounds $[Ru(tpy)(bpy)(OH_2)](ClO_4)_2$ (**1**), $[Ru(tpy)(bpy\text{-}OMe)(OH_2)](ClO_4)_2$ (**2**), and $[Ru(tpy)(bpy\text{-}CO_2H)(OH_2)](ClO_4)_2$ (**3**) were prepared and purified as previously reported.[48] Acid solutions were prepared from concentrated HNO_3 (70%, ACS grade) and distilled, deionized water and were measured to have a pH of 1.07 and 0.05 for 0.1 M HNO_3, 1.0 M HNO_3, respectively.

Physical Methods. Electrochemical measurements were performed under anaerobic conditions and recorded with a Princeton Applied Research VersaStat 3 potentiostat, a glassy carbon working electrode (diameter = 3 mm), and a [Ag]/[AgCl] reference electrode (3 M NaCl; 210 mV vs NHE). All potentials reported herein are referenced to a normal hydrogen electrode (NHE). Electrochemistry experiments carried out at variable pH values were carried out in appropriate buffered solutions with I = 0.1 M ([analyte] = ~1 mM), except at pH 0, where 1.0 M HNO_3 was used ([analyte] = ~1 mM). Electronic spectroscopy data were collected on a Varian Cary 5000 UV−vis spectrophotometer. Kinetics measurements were performed by stopped-flow methods using a Hi-Tech Scientific SFA-20 coupled to the Cary 5000 spectrometer, and absorbance versus time traces were collected at appropriate wavelengths. Unless otherwise stated, rate constants were determined by fitting absorbance versus time traces using the kinetics-fitting algorithm within the Varian Cary WinUV Kinetics Application [Version 3.00(182)] software package. An average of 10 trials was used to determine reported values of k_1-k_2 until standard deviations of less than 10% were achieved.

Dioxygen evolution data were recorded using a custom-built apparatus consisting of a 10-mL round-bottom flask equipped with a septum and a threaded side arm for insertion of the probe; the total working volume is 16.8 mL. In a typical experiment, the flask was charged with a solution of $(NH_4)_2[Ce(NO_3)_6]$ (CAN) in 3.0 mL of the acid solution (13 mM) and the headspace was then purged with $N_{2(g)}$ for ca. 20 min until a stable reading was obtained. Note that the CAN solution was not purged to maintain dioxygen saturation of the reaction solution so that a rapid response to dioxygen evolution could be measured. A deaerated solution containing the catalyst was then injected through a rubber septum resulting in a catalyst concentration of 7×10^{-5} M. The solution was stirred in a temperature modulated oil bath at 30 ± 2 °C for the duration of the experiment. Dioxygen evolution was monitored every 10 s with an optical probe (Ocean Optics FOXY-OR125-AFMG) and a multifrequency phase fluorimeter (Ocean Optics MFPF-100) calibrating using N_2 purging as a zero point and air as 20.9%. Raw data from the sensor were collected by the TauTheta Host Program and then converted into the appropriate calibrated O_2 sensor readings in "$\%O_2$" by the OOISensors application.

Separate solutions of **1** and CAN in 0.1 M HNO_3 were prepared and taken up in separate syringes for the ESI-MS experiments and directed to the capillary for ionization (combined flow rate = 50 μL/min). All mass spectra were recorded on a Waters Micromass Q-Tof Micro mass spectrometer or Agilent Technologies 6520 Accurate-Mass Q-TOF LC/MS spectrometer. Instrument parameters were optimized to maximize observed spectra: capillary voltage (3200 V); source temperature (100 °C); desolvation temperature (300 °C); desolvation flow rate (250 L/h); cone voltage (20 V); collision voltage (1 V); quadrupole ion energy (2 V).

The $H_2{}^{18}O$ labeling studies were performed using water containing 9.87% $^{18}OH_2$ on a weight basis prepared from 98.7% $^{18}OH_2$ purchased from Cambridge Isotopes Laboratories. The reactions were performed in the same apparatus as used for the dioxygen evolution studies. In a typical experiment, a solution of CAN (0.11 M) in HNO_3 solutions was degassed by thoroughly purging the solution and headspace with dinitrogen until a stable dioxygen reading was obtained (*ca.* 30 min). A deaerated solution of the catalyst dissolved in H_2O was then injected via syringe into the stirring CAN solution to achieve catalyst concentrations of $\sim 3 \times 10^{-4}$ M; the additional $^{16}OH_2$ content was taken into account. After the dioxygen reading had stabilized indicating the stoichiometric consumption of CAN, several 10−20 μL samples of the headspace gases were directly injected into a Varian 210 GC/MS Ion Trap containing a Molsieve 5A gas separation column and an ion trap set to focus on ions within the *m*/*z* 20−80 range. Traces of individual ions were determined by extracting the desired *m*/*z* value from the spectrum; relative concentrations of isotopes were determined by integrating the area under the signal of the appropriate extracted *m*/*z* value. The introduction of atmospheric dioxygen into the GC/MS apparatus was accounted for by using the measured O_2/N_2 ratio of pure N_2 (extracted from the reaction vessel without the catalyst) to correct for the $^{32}O_2$ signal during the catalytic runs. Mixing ratios of NO_2 were monitored by optical absorption at 405 nm using cavity ring-down spectroscopy (CRDS); the spectrometer has been described in detail elsewhere.[50] Each experiment involved the initial sampling of the headspace of a reaction flask containing a 1.0 M HNO_3 solution of CAN (2.0 mL). After a baseline response was obtained, a sparged solution containing the catalyst was added

(49) Hoertz, P. G.; Staniszewski, A.; Marton, A.; Higgins, G. T.; Incarvito, C. D.; Rheingold, A. L.; Meyer, G. J. *J. Am. Chem. Soc.* **2006**, *128*, 8234–8245.

(50) Paul, D.; Osthoff, H. D. *Anal. Chem.* **2010**, *82*, 6695–6703.

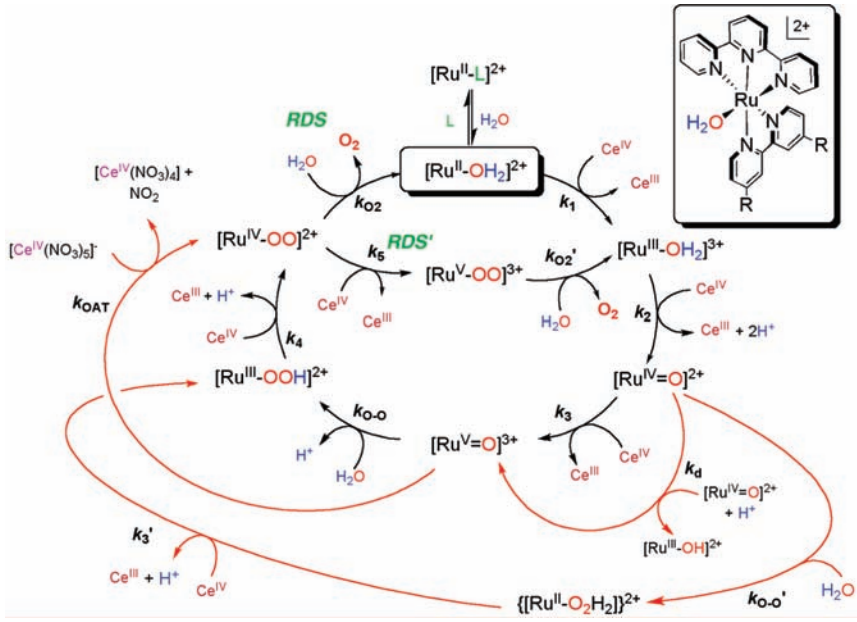

Figure 2. Summary of (possible) competing reaction pathways for **1**−**3** describing relevant (proton-coupled) electron-transfer steps, O−O bond formation, exclusion of dioxygen, and substrate binding (L = coordinating ligand; *e.g.*, Cl^-, MeCN; R = −H, **1**; −OMe, **2**; $-CO_2H$, **3**). Rate-determining steps (RDSs) for **1** and **3** (*RDS*), and **2** (*RDS′*) at pH 1 are indicated.[51]

to the sample chamber. All concentrations and conditions were the same as those for the dioxygen evolution experiments described above.

Results

This study was designed to develop a detailed description of the reaction landscape for a structurally related series of water oxidation catalysts **1**−**3** that contain variable electron density at the metal center. In this vein, each of the catalysts was evaluated by spectrophotometrically monitoring the Ce(IV)-driven oxidation of water (eq 1) in an acidic medium. We also tracked this reaction with an optical probe positioned in the reaction headspace as a secondary means of quantifying the catalytic activity. ESI-MS and UV−vis spectroscopy were used to help structurally identify catalytic intermediates, rate constants for key (proton-coupled) electron-transfer steps were determined by stopped-flow methods, and the source of O-atoms in dioxygen liberated during the reactions was verified by $^{18}OH_2$-labeling experiments.

$$4Ce(IV) + 2H_2O \xrightarrow{\text{catalyst}} 4Ce(III) + O_{2(g)} + 4H^+ \qquad (1)$$

Our mechanistic studies were designed to examine whether **1** adheres to the "acid−base" mechanism (denoted by black arrows in Figure 2) aligned with the scheme documented by Meyer et al., for **IV**.[31,46] The reaction pathway mediated by **IV** begins with two consecutive PCET steps to form $[Ru^{IV}{=}O]^{2+}$. A subsequent oxidation process generates the highly electrophilic $[Ru^{V}{=}O]^{3+}$ fragment that interacts with water to undergo the requisite O−O bond formation step, k_{O-O}, to form $[Ru^{III}{-}OOH]^{2+}$, which collapses to $[Ru^{IV}{-}OO]^{2+}$ following another PCET step, k_4.[52] The dioxygen ligand of this species can then be displaced by water to regenerate the catalyst in 0.1 M HNO_3 (i.e., k_4); alternatively in 1.0 M HNO_3, the one-electron oxidation of $[Ru^{IV}{-}OO]^{2+}$ (i.e., k_5) occurs followed by the rapid reductive elimination of dioxygen and subsequent coordination of water. The rate-determining step (RDS) in 0.1 M HNO_3 is assigned as k_{O2} within the "Ru(II)/Ru(V) cycle", while k_5 represents the RDS in the "Ru(III)/Ru(V) cycle" in 1 M HNO_3.

While our initial set of measurements suggested that **1**−**3** do, in large part, follow this same "acid−base" mechanism (i.e., nucleophilic attack of $[Ru^{V}{=}O]^{3+}$ by water), there are certain aspects of reactivity that diverge from that of **IV**. We have rationalized that this discrepancy arises not only because of a difference in the position of the RDS but also because of supplementary reaction cycles, in certain cases, that include disproportionation pathways and oxygen abstraction from CAN (denoted by red arrows in Figure 2).[53] Our experiments described herein shine light on the fact that the accessibility of each of these pathways is affected not only by the electron density at the metal but also by reaction conditions. The following sections detail our interpretation of the reactivity of **1**−**3**, which balances the thermodynamic demands of accessing the Ru(V) redox level, the electrophilicity of the high-valent [Ru=O] fragment, the acid medium, and the presence of CAN.

Structural Identity of the Active Site. There has been a general lack of solidarity in the literature over the past three decades over whether **1** is a *bona fide* water oxidation catalyst.[13,28,31] This controversy is presumably rooted in the fact that water oxidation is not observed upon generation of $[Ru^{IV}{=}O]^{2+}$ in solution,[54] and the $[Ru^{IV}{=}O]^{2+}$ form of **1** may not be capable of undergoing electron transfer with CAN ($E_{1/2}$, Ce(IV)/Ce(III) = 1.45 V vs NHE; Figure S1) due to the inaccessible $[Ru^{V}{=}O]^{3+}/[Ru^{IV}{=}O]^{2+}$ redox couple ($E_{1/2} \approx$ 1.60−1.80 V[30,48]). Moreover, the identification of the $[Ru^{V}{=}O]^{3+}$

(51) We do not rule out the possibility of $[Ru^{II}{-}OOH]^+$ being formed during the k_{O-O}' step.
(52) Specific bonding arrangement of peroxo Ru(IV) complexes is discussed in a later section.
(53) k_{OAT} represents an "O-atom transfer" (OAT) step that refers strictly to the abstraction of an O-atom from CAN by the Ru catalyst, and does not necessarily imply a static formal charge of the O-atom before and after the reaction.
(54) Takeuchi, K. J.; Thompson, M. S.; Pipes, D. W.; Meyer, T. J. *Inorg. Chem.* **1984**, *23*, 1845–1851.

Table 1. Summary of Electrochemical Data and Spectrophotometrically Determined pK_a Values for **1**−**3**

	$E_{1/2}$ (V vs NHE)[a]			pK_a[d]	
Complex	Ru(III)/Ru(II)[b]	Ru(IV)/Ru(III)[b]	Ru(V)/Ru(IV)[b]	$[Ru^{II}-OH_2]^{2+}$	$[Ru^{III}-OH_2]^{3+}$
1	1.04	1.23	1.80	10.5	1.7[e]
2	0.91	1.24	1.77	11.2	3.2
3	1.16	—[c]	1.89	10.4	1.2

[a] Samples (1 mM) dissolved in 0.1 M HNO_3 were measured at 50 mV/s and referenced to a Ag/AgCl (3 M NaCl) electrode at 25 ± 2 °C; Ru(V)/Ru(IV) value determined by square wave voltammetry. [b] Assignment of proton-coupled oxidation waves are indicated: Ru(II) = $[Ru^{II}-OH_2]^{2+}$; Ru(III) = $[Ru^{III}-OH_2]^{3+}$; Ru(IV) = $[Ru^{IV}=O]^{2+}$; Ru(V) = $[Ru^{V}=O]^{3+}$. [c] Not observed. [d] [Ru] = 5.0 × 10^{-5} M in buffered phosphate solution. [e] Previously reported.[54]

species prior to the onset of catalysis at the electrode can be ambiguous in certain conditions. There has been speculation that the decomposition of Ru coordination complexes into catalytically active nanoparticles broadly formulated as $RuO_2 \cdot xH_2O$ is the source of dioxygen formation. We have ruled out this possibility by a series of control experiments,[48] the full recovery of the catalyst following the addition of 30 equiv of CAN to **1**−**3** (vide infra), and the fact that RuO_2 forms catalytically inactive RuO_4 at the Ce/Ru molar ratio relevant to our experiments.[55,56]

While there now appears to be general agreement that **1** is, indeed, a water oxidation catalyst,[25,33,48] the nature of the active site remains an open question. Given that dioxygen formation has been observed in reactions catalyzed by $[Ru(tpy)(bpy)Cl]^{+}$[28] and seven-coordinate Ru(II) compounds with strained ligand environments,[32] we considered the possibility that **1**−**3** could undergo an expansion of the primary coordination sphere to retain a Ru−anion bond. A series of experiments carried out in our laboratories[48] and those of Sakai et al.[33] and Meyer et al.,[29] however, have verified that the catalytically active forms of **1**−**3** are the $[Ru-OH_2]^{2+}$ species. In fact, **1**−**3** each exist in a dynamic equilibrium with coordinating ligands (e.g., MeCN, Cl^-, SO_4^{2-}) that effectively suppress the catalytic activity of these Ru complexes.[33,48] Consequently, these coordinating species were avoided in this study to avoid complicating our interpretation of the mechanistic behavior. Each of the samples were prepared in bulk and analyzed for purity by ^{1}H NMR spectroscopy, elemental analyses, and UV−vis spectroscopy prior to analysis.

Electrochemical Behavior. The electron-donating and -withdrawing characters of the bpy-OMe and bpy-CO_2H ligands are evidenced by the respective cyclic voltammograms for **1**−**3** in 0.1 M HNO_3 (Table 1; Figures S2−S3). An oxidative sweep for **1** produces two closely spaced single-electron redox processes at +1.04 and +1.23 V, along with a third signal at ∼+1.80 V, which occurs with the onset of a rapid increase in peak current due to the concomitant catalytic oxidation of water. The close proximity of the first two signals is a consequence of (proton-coupled) electron-transfer processes stabilizing the higher redox levels of the complexes (e.g., the first two oxidation steps generate $[Ru^{III}-OH_2]^{3+}$ and $[Ru^{IV}=O]^{2+}$, respectively). The reversible $[Ru^{III}-OH_2]^{3+}/[Ru^{II}-OH_2]^{2+}$ wave occurs at 1.04, 0.91, and 1.16 V for **1**−**3**, respectively, in accordance with the variable electron-donating character of the substituents. The variance of the respective $[Ru^{IV}=O]^{2+}/[Ru^{III}-OH_2]^{2+}$ processes for **1** and **2** is much less pronounced (i.e., *ca.* 30 mV), which reflects a diminished level of π-backbonding in stabilizing the Ru(III) redox level. Two distinct oxidation processes are not observed in the voltammograms for **3**, which is ascribed to slow reaction kinetics at the electrode surface.[57] A more pronounced variance (*ca.* 120 mV) is observed for the $[Ru^{V}=O]^{3+}/[Ru^{IV}=O]^{2+}$ couple for the series (the $E_{1/2}$ for this process was resolved by square-wave voltammetry; Figure S4).

The Pourbaix diagrams for **1**,[54] **2**, and **3** reveal that the $[Ru^{III}-OH]^{2+}/[Ru^{II}-OH_2]^{2+}$ and $[Ru^{IV}=O]^{2+}/[Ru^{III}-OH]^{2+}$ redox processes each change by approximately 59 mV per pH decade over a large pH range (Figure 3). Deviations from Nernstian behavior are observed in regions where the dissociation of a proton can be affected; i.e., at relevant pK_a values. The peak separations of the Ru(III)/Ru(II) and Ru(IV)/Ru(III) redox couples for **2** are approximately 200 mV over the pH 3.1−11.2 range. At pH < 3.1, the oxidation of **2** is not associated with the loss of a proton based on the pH-independent behavior of the $[Ru^{III}-OH_2]^{3+}/[Ru^{II}-OH_2]^{2+}$ redox couple. Consequently, the subsequent oxidation step is accompanied with the loss of two protons (i.e., $[Ru^{IV}=O]^{2+}/[Ru^{III}-OH_2]^{3+}$) in strongly acidic media. This assignment is corroborated by the slope of −118 mV/pH below pH 3.1 in Figure 3, as well as independent spectrophotometric measurements (Figure S7). Compound **2** is deprotonated at pH > 11.2 resulting in the pH-independent oxidation of the Ru(II) center until pH 12; the first oxidation wave at pH > 12 is assigned as a two-electron, one-proton event (*i.e.*, $[Ru^{IV}=O]^{2+}/[Ru^{II}-OH]^{1+}$). The $[Ru^{V}=O]^{3+}/[Ru^{IV}=O]^{2+}$ redox couple remains relatively constant at ∼1.77 V vs NHE over the pH 0−13 range.

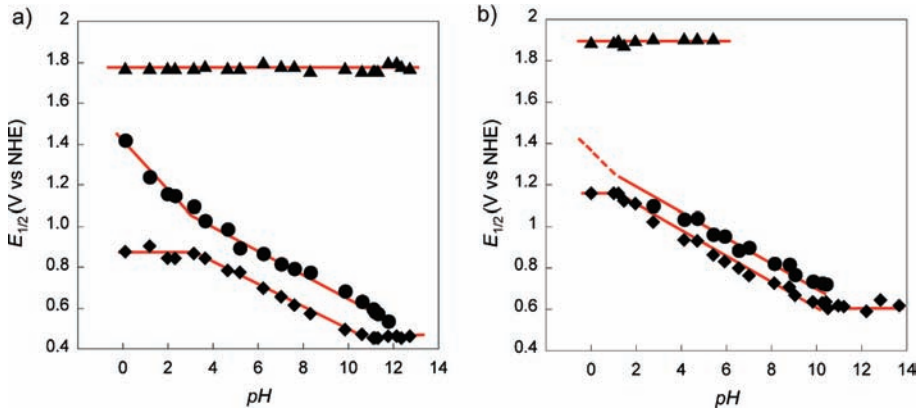

Figure 3. Plot of the pH-dependence on the electrochemical behavior of (a) **2** and (b) **3**. The red solid lines indicate trends in data; diamonds, circles, and triangles correspond to the Ru(III)/Ru(II), Ru(IV)/Ru(III), and Ru(V)/Ru(IV) redox couples, respectively. The silent Ru(IV)/Ru(III) wave at low pH for **3** is ascribed to slow kinetics at the electrode. (The Pourbaix diagram for **1** is reported elsewhere.[54])

Table 2. Electron-Transfer Rate Constants in 0.1 M HNO_3 at 25 ± 2 °C

Reaction Step	Reaction Description	Compound[a] 2	1	3
k_1 (M^{-1} s^{-1})	$[Ru^{II}—OH_2]^{2+} \rightarrow [Ru^{III}—OH_2]^{3+}$ + H^+ ($Ce^{IV} \rightarrow Ce^{III}$)	1.7×10^5	4.4×10^4	rapid[b]
k_2 (M^{-1} s^{-1})	$[Ru^{III}—OH_2]^{3+} \rightarrow [Ru^{IV}=OH_2]^{3+}$ + H^+ ($Ce^{IV} \rightarrow Ce^{III}$)	4.6×10^3	6.6×10^3	3.3×10^5

[a] [Catalyst] = 5×10^{-5} M. [b] Time scale too short to be resolved with our instrument (i.e., $>10^6$ M^{-1} s^{-1}).

The Pourbaix diagram for **3** displays some minor deviations relative to that of **1** and **2**. For instance, a smaller difference (*ca*. 90 mV) is observed between the first two successive PCET events over the 1.2 < pH < 10.5 range. The first oxidation wave is pH-independent at 10.5 > pH < 1.2. The $[Ru^{IV}=O]^{2+}$/$[Ru^{III}—OH]^{2+}$ couple was not observed at pH < 2.8 using various electrochemical conditions and techniques (e.g., differential pulse voltammetry, square-wave voltammetry). While we considered the possibility that the Ru(III) level is not stable and undergoes disproportionation,[31,58] our titration experiments do not support this scenario; consequently, this silent redox couple is attributed to slow reaction kinetics at the electrode.[57] The $[Ru^{V}=O]^{3+}$/$[Ru^{IV}=O]^{2+}$ couple for **3** was observed at *ca*. 1.9 V vs NHE over a significant pH region.

The $E_{1/2}$ vs pH plots facilitate the extrapolation of the pK_a values of the aqua ligand for **1**−**3**, which are shown to track with electron density at the metal center; i.e., pK_a increases for **3**, **1**, and **2**, respectively (Figure 3). These values were independently verified by spectrophotometric titrations of the respective complexes in buffered solutions (Table 2 and Figure S5).

Spectroscopic Signatures for Well-Defined Redox Levels of 1−**3.** The absorbance profiles of the three different valence forms found early in the catalytic cycle (i.e., $[Ru^{II}—OH_2]^{2+}$, $[Ru^{III}—OH_2]^{3+}$, and $[Ru^{IV}=O]^{2+}$ in Figure 2) for **1**−**3** are provided in Figure 4. The lowest redox level for all three catalysts exhibits the signature metal-to-ligand charge-transfer (MLCT) band between 470 and 500 nm along with higher-energy ligand-based $\pi-\pi^*$ transitions. The oxidation of each of these complexes results in a bleaching of this broad visible band leaving prominent spectral features in the UV region. The respective Ru(III) and Ru(IV) species were each generated by adding stoichiometric equivalents of CAN to 5.0×10^{-5} M solutions of the respective complexes in 0.1 M HNO_3; clear isosbestic points (Table S1) were observed in titration experiments with **1**−**3** and signal the successive stoichiometric conversion of $[Ru^{II}—OH_2]^{2+}$ to $[Ru^{III}—OH_2]^{3+}$ and $[Ru^{IV}=O]^{2+}$ (Figures S6−S8). A detailed listing of the spectroscopic features in Figure 4 is provided in Table S2.

The relative stabilities of the lowest redox level (i.e., Ru(II)) for each of the catalysts in solution (monitored by tracking the bleaching of the MLCT band) are progressively higher for **2**, **1**, and **3**, respectively. This behavior is more pronounced in stronger acids (e.g., 1 M HNO_3), where **2** is rapidly oxidized to Ru(III) via the series of reactions described in eqs 2−4.[59] Complex **1** undergoes this same decomposition at a slower rate corresponding to a pseudo-first-order rate coefficient of 1.8×10^{-3} s^{-1}, while **3** is stable in solution over a period of several weeks. Consequently, all of our electron-transfer rates and catalytic measurements were carried out in 0.1 M HNO_3 to (i) suppress the spontaneous decomposition of **1** and **2** in solution at lower pH values and (ii) to evade the formation of complex hydroxides when CAN is dissolved in aqueous media at higher pH levels. We also note that determination of rate constants for subsequent reaction steps (e.g., k_3, k_{O-O}) at pH 0 is impeded by the strong absorbance of 1 M HNO_3 at <350 nm masking the absorbance region of interest.

$$2[Ru^{II}—OH_2]^{2+} + NO_3^- + 3H^+ \rightleftharpoons 2[Ru^{III}—OH_2]^{3+} + HNO_2 + H_2O \quad (2)$$

$$[Ru^{II}—OH_2]^{2+} + NO_3^- + H^+ \rightleftharpoons [Ru^{IV}=O]^{2+} + HNO_2 + H_2O \quad (3)$$

$$[Ru^{II}—OH_2]^{2+} + [Ru^{IV}=O]^{2+} + 2H^+ \rightarrow 2[Ru^{III}—OH_2]^{3+} \quad (4)$$

The electron-withdrawing character imparted by the $—CO_2H$ substituents is clearly demonstrated by the instability or reactivity of the $[Ru^{IV}=O]^{2+}$ form of **3** in solution. The $[Ru^{IV}=O]^{2+}$ species that is generated in solution undergoes a slow decomposition to species with spectral features indicative of divalent and trivalent Ru. The decay of the $[Ru^{IV}=O]^{2+}$ complex was found to be second-order in [**3**], thereby indicating a bimolecular decomposition pathway. On this basis, we attribute this process to a disproportionation reaction step (k_d) that forms $[Ru^{V}=O]^{3+}$ and $[Ru^{III}—OH]^{2+}$ in the acid medium ($k_d = 1.2$ M^{-1} s^{-1}; Figure S9); the $[Ru^{V}=O]^{3+}$ species, in turn, is presumed to go on to react with water to form $[Ru^{III}—OOH]^{2+}$ via k_{O-O}. The implication of this result is that a Ru(V) species is generated after the addition of only 2 equiv of CAN to **3**, thus providing access to the k_{O-O} pathway. Moreover, evidence for the k_{O-O}' step, which involves dioxygen bond formation at a Ru(IV) center, is provided by the onset of a signal at $\lambda_{max} \approx 490$ nm, which we

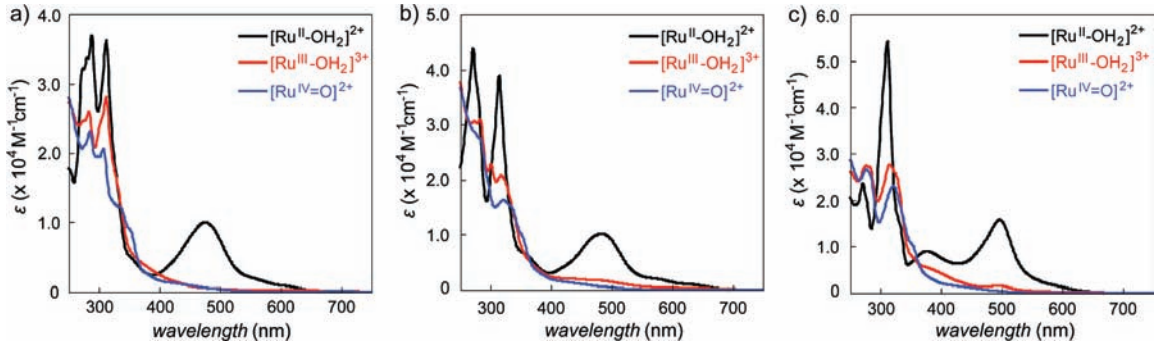

Figure 4. Electronic absorption spectra of the $[Ru^{II}—OH_2]^{2+}$, $[Ru^{III}—OH_2]^{3+}$ and $[Ru^{IV}=O]^{2+}$ redox levels for (a) **1**, (b) **2**, and (c) **3**. The Ru(III) and Ru(IV) redox levels were generated by stoichiometric titrations of the complex (5.0×10^{-5} M) with CAN in 0.1 M HNO_3.

assign as the formation of the $[Ru^{II}—O_2H_2]^{2+}$ (or $[Ru^{II}—OOH_2]^{+}$) species. (A second disproportionation reaction generating the $[Ru^{II}—OH_2]^{2+}$ species according to eq 5 was also considered but is not supported by other titration experiments; vide infra.) Both of these reaction pathways deviate from the acid−base mechanism and not only show a thermodynamically favorable route for the formation of a $[Ru^{V}=O]^{3+}$ species in these titration experiments and but also provide evidence that nucleophilic attack of an electron-deficient $[Ru^{IV}=O]^{2+}$ by water can occur.

$$2[Ru^{III}—OH_2]^{3+} \rightleftharpoons [Ru^{II}—OH_2]^{2+} + [Ru^{IV}=O]^{2+} + 2H^{+} \quad (5)$$

Monitoring the spectral changes of **1** reveals some minor spectral changes that we assign as this same disproportionation process at a slow rate of $\sim 0.3\ M^{-1}\ s^{-1}$; there is also evidence that this process can also occur at an even slower rate for **2**. Our spectroscopic data do not support the occurrence of k_{O-O}' for **1** or **2**.

Rates of Electron Transfer and O−O Bond Formation. Intermolecular electron-transfer steps k_1-k_3 and dioxygen bond formation step k_{O-O} were determined (where applicable) by stopped-flow methods in 0.1 M HNO_3 by adding equimolar quantities of CAN to the Ru(II) or Ru(III) forms of each of the three catalysts (Table 2). The first two electron-transfer steps can be determined by monitoring the rates of the reactions according to eqs 6−7.[29] The first electron-transfer step k_1 is rapid for each of the catalysts; k_2 is slower but still rapid, and follows the trend **3** > **1** > **2**. Both of these electron-transfer events are relatively fast for all of the catalysts and do not represent RDSs within the respective catalytic cycles.

$$-\frac{d[Ru^{II}—OH_2]}{dt} = k_1[Ru^{II}—OH_2][CAN] \quad (6)$$

$$-\frac{d[Ru^{III}—OH_2]}{dt} = k_2[Ru^{III}—OH_2][CAN] \quad (7)$$

We set out to extract the value of k_3 by tracking the rate of CAN or $[Ru^{IV}=O]^{2+}$ decay (and/or the onset of a distinctive $[Ru^{V}=O]^{3+}$ species) following the addition of 1 equiv of CAN to the respective $[Ru^{IV}=O]^{2+}$ forms of the catalysts (eq 8). A subsequent (slower) k_{O-O} step can then be extracted according to eq 9 using the corresponding integrated rate law described in eq 10 (A = absorbance at time t; A_o = absorbance at $t = 0$; A_∞ = absorbance at t_∞). This procedure was shown to be particularly effective for the analysis of single-site catalysts by Meyer et al.[29] but produced a disparate and often ambiguous set of results for each of the catalysts in this study. For instance, the combination of 1 equiv of CAN with the $[Ru^{IV}=O]^{2+}$ form of **1** did not produce distinct spectral changes that are consistent with an electron-transfer step and/or dioxygen formation, while trends corresponding to the formation of the ostensible $[Ru^{V}=O]^{3+}$ and $[Ru^{III}—OOH]^{2+}$ species do appear in the case of **2**. We therefore assign the reaction of CAN with $[Ru^{IV}=O]^{2+}$ as electron-transfer step k_3 for **2** in accordance with the acid−base mechanism. The subsequent k_{O-O} step for **2**, which is determined by monitoring the onset of a new species with a feature at 320 nm later in the reaction (Figure S10), occurs on a much slower time scale than that of k_3; i.e., k_3 and k_{O-O} are $3.7\ M^{-1}\ s^{-1}$ and $3 \times 10^{-5}\ s^{-1}$, respectively. This $[Ru^{III}—OOH]^{2+}$ species does not disproportionate to $[Ru^{IV}—OO]^{2+}$ and $[Ru^{II}—H_2O_2]^{2+}$ on a reasonable time scale (as was observed for **IV**).[60] We note that the measured k_{O-O} value is slower than k_{cat}, suggesting that (i) the second process that is occurring is not actually k_{O-O} or (ii) auxiliary reactions lead to an underestimation or misrepresentation of k_{O-O} (vide infra).

$$-\frac{d[Ru^{IV}=O]}{dt} = k_2[Ru^{IV}=O][CAN] \quad (8)$$

$$\frac{d[Ru^{III}—OOH]}{dt} = k_{O\text{-}O}[Ru^{III}—OOH] \quad (9)$$

$$\ln\left(\frac{A - A_o}{A_\infty - A_o}\right) = -k_{O\text{-}O}t \quad (10)$$

The addition of 1 equiv of CAN to the $[Ru^{IV}=O]^{2+}$ form of **1** results only in a slightly lower intensity of the absorbance profile (Figure S11). Two possible interpretations of these data include the following: (i) the electron-transfer reaction is slow or nonexistent; or (ii) the $[Ru^{IV}—OO]^{2+}$ species is generated at a faster rate than the $[Ru^{V}=O]^{3+}$ level. The slow reaction step k_3 for **1** relative to **2** is supported by the greater thermodynamic demands associated with oxidizing the Ru(IV) center. The rapid generation of the $[Ru^{IV}—OO]^{2+}$ species is consistent with a slow k_d step followed by relatively faster k_{O-O}/k_4 steps and/or a fast oxygen-atom transfer (OAT) step, k_{OAT}. This scenario implies that the $[Ru^{III}—OH]^{2+}$ species that is formed by k_d would be quickly regenerated to the $[Ru^{IV}=O]^{2+}$ species; i.e., the dominant species in solution under these conditions would be $[Ru^{IV}=O]^{2+}$ and $[Ru^{IV}—OO]^{2+}$, thus rendering minor spectroscopic changes.

In the case of **3**, the addition of 1 equiv of CAN to the $[Ru^{IV}=O]^{2+}$ form leads to a successive decrease and increase in absorbance at 320 nm. While this behavior is expected if we are tracking only k_3 and k_{O-O}, there are two additional pathways that diverge from the $[Ru^{IV}=O]^{2+}$ species that may be operative based on the observed spectral changes (e.g., k_{O-O}' and k_d). Because electron-transfer step k_3 is expected to be very slow under these conditions due to the energetic demands of oxidizing a Ru(IV) center, the spectral changes are attributed to the formation of the $[Ru^{III}—OOH]^{2+}$ species by means of the independent k_d/k_{O-O} and k_{O-O}'/k_3' pathways. The former is supported by the spectral trends at 320 nm, which would correspond to $k_d \approx 2\ M^{-1}\ s^{-1}$ and $k_{O-O} = 1 \times 10^{-4}\ s^{-1}$ (the latter is expected to be faster than **2**, because of the greater susceptibility to nucleophilic attack by water, but is again slower than k_{cat}, underscoring that competing pathways may lead to a false representation of this value). The k_{O-O} step is supported by the gradual buildup of a species characterized by $\lambda \approx 490$ nm that we assign as the $[Ru^{II}—O_2H_2]^{2+}$ complex ($[Ru^{II}—OOH]^{+}$ is not ruled out), followed by a rapid decrease concomitant with the onset of a signal at 690 nm, which we assign as $[Ru^{III}—OOH]^{2+}$ (Figure S12). The disproportionation reaction

(55) Kiwi, J.; Grätzel, M.; Blondeel, G. *J. Chem. Soc., Dalton Trans.* **1983**, 2215–2216.
(56) Mills, A. *J. Chem. Soc., Dalton Trans.* **1982**, 1213–1216.
(57) Dovletoglou, A.; Adeyemi, S. A.; Meyer, T. J. *Inorg. Chem.* **1996**, *35*, 4120–4127.
(58) Masllorens, E.; Rodriguez, M.; Romero, I.; Roglans, A.; Parella, T.; Benet-Buchholz, J.; Poyatos, M.; Llobet, A. *J. Am. Chem. Soc.* **2006**, *128*, 5306–5307.
(59) Moyer, B. A.; Meyer, T. J. *J. Am. Chem. Soc.* **1979**, *101*, 1326–1328.
(60) A direct comparison of k_{O-O} values of **IV** to **2** is made difficult by the disparate rates of disproportionation, affecting the curvature of the absorbance versus time traces.

Table 3. Spectrophotometric Determination of Key Rate Constants for **1**−**3** at 25 ± 2 °C[a]

	0.1 M HNO_3		1 M HNO_3	
Complex	rate expression	k_{cat}[b]	rate expression	k_{cat}[b]
1	k_{cat}[**1**]	6.6×10^{-4} s^{-1} (1100)	k_{cat}[**1**][CAN]	22 M^{-1} s^{-1} (210)
2	k_{cat}[**2**][CAN]	1.0 M^{-1} s^{-1} (460)	k_{cat}[**2**][CAN]	180 M^{-1} s^{-1} (3)
3	k_{cat}[**3**]	4.3×10^{-4} s^{-1} (1600)	k_{cat}[**3**][CAN]	9.2 M^{-1} s^{-1} (500)

[a] [Ru] = (1.0−9.0) × 10^{-5} M; [CAN] = (3.0−27) × 10^{-4} M; k_{cat} determined by monitoring the decay of CAN at 360 nm in the dark. [b] $t_{1/2}$ indicated in parentheses in units of s; second-order $t_{1/2}$ values correspond to $\ln(2)/k_{cat}[CAN]_i$.

described in eq 5 is ruled out on the basis that the CAN present in solution in this experiment would quickly regenerate the $[Ru^{III}-OH_2]^{3+}$ that is formed during the k_d step. We caution that the credibility of our measured "k_{O-O}" value is compromised by these competitive pathways in solution.

Spectrophotometric Determination of k_{cat} for 1−3. The consumption of CAN was monitored in 0.1 and 1.0 M HNO_3 at 360 nm to determine the observed catalytic rates (k_{cat}) for the reaction described in eq 1; relevant data are collected in Table 3. A typical reaction involves adding 30 equiv of CAN to a (1−9.0) × 10^{-5} M solution of the catalyst.

The spectrophotometric determination of k_{cat} for **1** and **3** reveals a dominant pathway that follows a zero-order dependence in [CAN] over the initial stages of the reaction. (Under catalytic conditions for **3** in 0.1 M HNO_3, a visible precipitate forms in the reaction flask; this process is concentration dependent.) A linear relationship between initial reaction rates ($k_{initial}$) and [Ru] indicates that the catalytic behavior follows the rate expression $rate = k_{cat}$[Ru] (determined by the slopes in Figure 5a and 5c), which implies that the RDS is not associated with an oxidation or OAT step. Considering that the oxidation of the purported $[Ru^{IV}-OO]^{2+}$ complexes for **1** and **3** are unlikely based on thermodynamic considerations, and that k_{O-O} is presumably faster for **3** than **1** (yet k_{cat} follows an opposite trend), we assign the RDS as k_{O2} for both catalysts, which is analogous to that of **IV**. This result indicates that, under conditions of excess CAN, the k_3 step is enhanced due to a combination of Nernstian behavior (e.g., E_{red} is 1.43 and 1.54 V with 3 and 30 equiv of CAN in 0.1 M HNO_3, respectively) and the $[Ru^{III}-OOH]^{2+}$ species being siphoned off by the excess oxidant in solution.

The extraction of k_{cat} for **2**, on the other hand, reveals behavior that is non-zero order in [CAN][61] and follows the expression $rate = k_{cat}$[**2**][CAN], where $k_{cat} = 1.0$ M^{-1} s^{-1} (Figures 5b and S13). This rate expression is aligned with the RDS being k_5 (k_3 is faster), which underscores how electronic parameters can affect the position of the RDS (the RDS is k_{O2} for **1**, **3**, **IV**,[29,31] and **V**[29,31] in 0.1 M HNO_3). The higher k_{cat} value for **2** compared to **1** and **3** also indicates that there is favorable dioxygen release from a Ru(V) level relative to a Ru(IV) center and/or the electron-donating groups help to labilize the (end-on[37] or side-on[29]) peroxo ligand. Note that the slope in Figure 5b does not pass through the origin, which suggests the possibility of competing reaction pathways (e.g., decomposition of CAN, k_{OAT}; vide infra).

A particularly telling outcome of these experiments is the spectral profiles that are converged upon at the end of the catalytic runs (Figure 6). The dominant species under catalytic conditions for **1** is consistent with a Ru(IV) complex (e.g., $[Ru^{IV}=O]^{2+}$ or $[Ru^{IV}-OO]^{2+}$), which is aligned with the significant energetic barriers associated with k_3 and k_{O2}. The time-dependent spectra for **2** do not converge on the $[Ru^{IV}=O]^{2+}$ complex and support the dominant species in solution being a $[Ru^{IV}-OO]^{2+}$ or Ru(V) species. The spectral difference may also reflect the stabilization of different bonding motifs of the

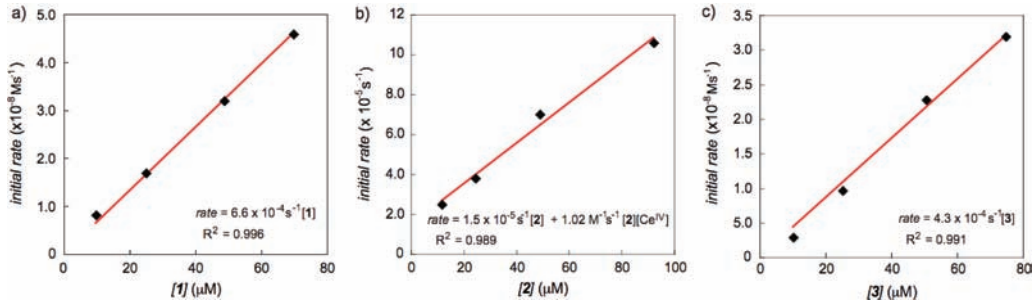

Figure 5. Spectrophotometric determination of k_{cat} (by monitoring the consumption of CAN at 360 nm) for (a) **1**, (b) **2**, and (c) **3** in 0.1 M HNO_3 at 25 ± 2 °C by tracking the initial rates ($\Delta t = 10$ min) of CAN consumption as a function of [Ru] following the addition of 30 equiv of CAN to the catalyst (see text for details).

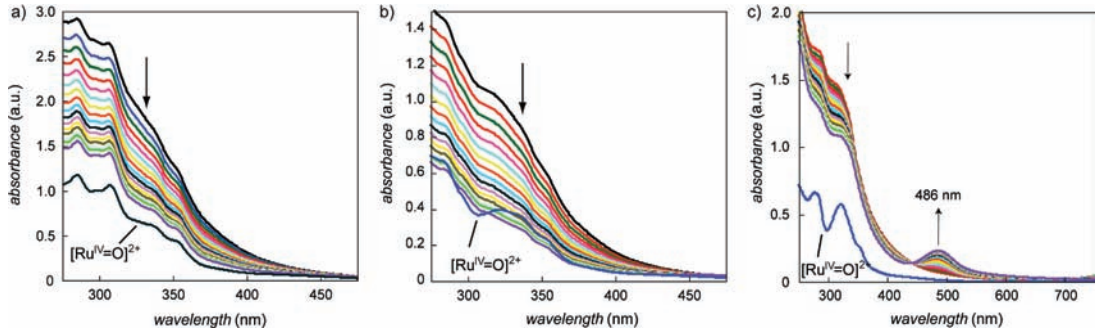

Figure 6. Spectral changes as a function of time following the addition of 30 equiv of CAN in 0.1 M HNO_3 for (a) **1** (5.0×10^{-5} M), (b) **2** (2.5×10^{-5} M), and (c) **3** (2.5×10^{-5} M). Spectra are measured in 60-min time intervals; arrows indicate trends in data. The spectra for the $[Ru^{IV}=O]^{2+}$ forms of each of the catalysts are provided as a benchmark.

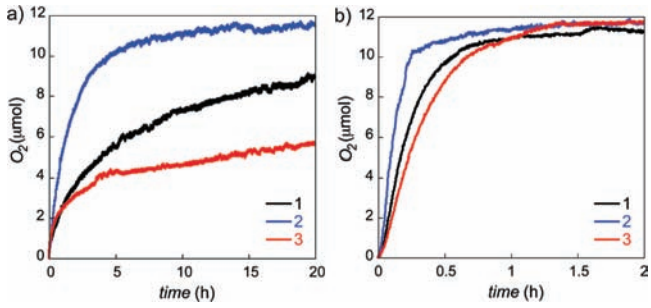

Figure 7. Dioxygen evolution traces for **1**−**3** in (a) 0.1 M HNO_3, (b) 1 M HNO_3 ([Ru] = 7.0 × 10^{-5} M; v_{acid} = 3 mL; [CAN] = 13 mM).

$[Ru^{IV}{-}OO]^{2+}$ complex late in the catalytic cycle relative to **1** (i.e., end-on versus side-on;[29,37] eq 11). In the case of **3**, the spectral changes are distinctive in that a signal at 486 nm begins to emerge over time. This is an intriguing result because this band is a signature of a Ru(II) MLCT transition, but the Ru(II) complexes specified in Figure 2 are all susceptible to rapid oxidation in the presence of CAN. Consequently, we assign the onset of this signal to the stabilization of the Ru(II) resonance form of the side-on peroxo/dixoygen complex (eq 12) by the electron-withdrawing groups. Taking these results into collective consideration indicates that the generic assignment of k_{O2} as the RDS may be complicated by the precise bonding arrangement of the Ru(IV) species late in the catalytic cycle; this specific feature currently lacks clarity in the literature.[29,37]

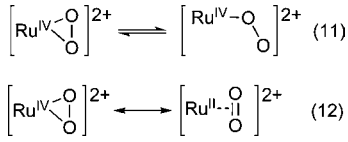

(11)

(12)

We observe a significant increase in the rate of consumption of CAN in 1.0 M HNO_3 for all of the catalysts, where each follow the expression rate = k_{cat}[Ru][CAN] (Table 3). The k_{cat} value is particularly rapid for **2** (180 M^{-1} s^{-1}), while **1** is only slightly faster than that of **3**. (There is no observable precipitate for **3** under these conditions.) We attribute this trend to k_5 being rate-determining for all three catalysts under these conditions (consistent with that of **IV**[31]), so that the k_{cat} is dictated by the accessibility of the Ru(V) level; i.e., **2** > **1** > **3**. The disparate rates at pH 0 and 1 highlight how reaction conditions can affect catalytic activity given that k_3 and k_5 are 3.7 and 1.0 M^{-1} s^{-1} in 0.1 M HNO_3, respectively, but k_{cat} in 1.0 M HNO_3 is 180 M^{-1} s^{-1}.

Determination of $k_{obs\text{-}O2}$ by Monitoring Dioxygen Evolution. Time-dependent dioxygen evolution measurements were measured for each of the complexes using a fluorescent probe in the headspace of the reaction vessel (Figure 7a and Table 4). In contrast to the previous experiments, these trials require a large excess of CAN (i.e., ≥ 200 equiv) to generate a significant quantity of dioxygen in the headspace for a satisfactory signal-to-noise level.

In 0.1 M HNO_3, the catalytic rate of dioxygen evolution ($k_{obs\text{-}O2}$) for **2** (1.5 × 10^{-4} s^{-1}) is approximately twice that of **1** (0.61 × 10^{-4} s^{-1}); both follow the expression *rate* = $k_{obs\text{-}O2}$[Ru] (zero-order in [CAN]) under pseudo-first-order conditions. Stoichiometric conversion of oxidizing equivalents to dioxygen are observed only for **2** over a 20-h period due in large part to the faster catalytic rates of **2**. While complications arise for measurements with **3** because the catalyst precipitates over the course of the reaction, catalysis persists following zero-order reaction behavior at ~3 × 10^{-9} M^{-1} s^{-1}. This behavior is ascribed to either slow dissolution of a catalytically active form of **3** or dioxygen formation at a nanoparticulate decomposition product. Over longer time periods, **1** and **3** may be able to mediate the complete consumption of CAN, though complications are likely to arise due to the instability of CAN in solutions over a period of days. In 1.0 M HNO_3, the rates of dioxygen evolution by all three catalysts are enhanced by more than an order of magnitude and follow the trend **2** > **1** > **3** (Figure 7b). For each of the catalysts, the amount of dioxygen evolved was expected to correspond to the amount of oxidant introduced into the reaction flask. In 0.1 M HNO_3, however, the amount of dioxygen formed is less than stoichiometric for **1** and **3** and greater for **2**. This provides strong evidence of an auxiliary reaction pathway involving a secondary O-atom source (i.e., k_{OAT}). This behavior also supports that the position of the RDS can be affected by pH (i.e., k_{O2} at pH 1 and k_5 at pH 0 for **1** and **3**).[29,46]

Table 4. Observed Rates of Dioxygen Evolution and Catalyst Efficiencies in HNO_3 at 30 ± 2 °C[a]

	0.1 M HNO_3		1.0 M HNO_3
Complex	$k_{cat\text{-}O2}$ (× 10^{-4} s^{-1})[b]	*Eff.* (%)[c]	$k_{cat\text{-}O2}$ (× 10^{-4} s^{-1})[b]
1	0.61	80	10
2	1.5	117	18
3	−[d]	50[d]	6.9

[a] Measured using a fluorescent optical probe in the headspace of the reaction vessel with 200 equiv of CAN; [Ru] = 7.0 (±0.03) × 10^{-5} M; [CAN] = 1.4 (±0.05) × 10^{-2} M; initial turnover frequencies are provided in Table S3. [b] Pseudo-first-order rate constant obtained by exponential fit of dioxygen evolution traces (±5%). [c] Catalyst efficiency is defined as the consumption of CAN resulting in stoichiometric equivalents of dioxygen (max 20 h; ±5%). [d] A precipitate forms over the course of the reaction leading to zero-order behavior in [Ru].

Electrospray Ionization Mass Spectrometric Analysis. Electrospray-ionization mass spectrometry (ESI-MS) is a soft ionization technique that has demonstrated the facility to probe reactions under *catalytic* conditions.[62−64] Generally, polar solvents function best for purposes of ESI-MS, and most instruments are well equipped to evaporate solvents with boiling points as high as water. While we are cognizant that neutral species are invisible to ESI-MS, viable intermediates in the catalytic pathways of **1**−**3** are anticipated to bear a charge enabling the ESI-MS study of native reactions at optimal concentrations or loadings. Also fortuitous is the fact that many of the catalytic intermediates in this study are characterized by unique empirical formulas that appear in a distinct region of the mass spectrum; thus, we are not faced, in most cases, with the tedious issue of delineating the overlapping spectroscopic

(61) We note that this same behavior was observed to a lesser extent for **1** and **3**; i.e., increasing concentrations of CAN leads to a slight enhancement of reaction rates. The implication of this result is that the rate law expression may be better described as a mixture of first- and second-order kinetic behavior; e.g., rate = k[Ru] + k'[Ru][CAN].

(62) Henderson, W.; McIndoe, J. S. *Mass Spectrometry of Inorganic and Organometallic Compounds*; John Wiley and Sons, Ltd.: Hoboken, NJ, 2005.
(63) Fenn, J. B.; Mann, M.; Meng, C. K. A. I.; Wong, S. F.; Whitehouse, C. M. *Science* **1989**, *246*, 64–71.
(64) Chisholm, D. M.; Oliver, A. G.; McIndoe, J. S. *Dalton Trans.* **2009**, *39*, 364–373.

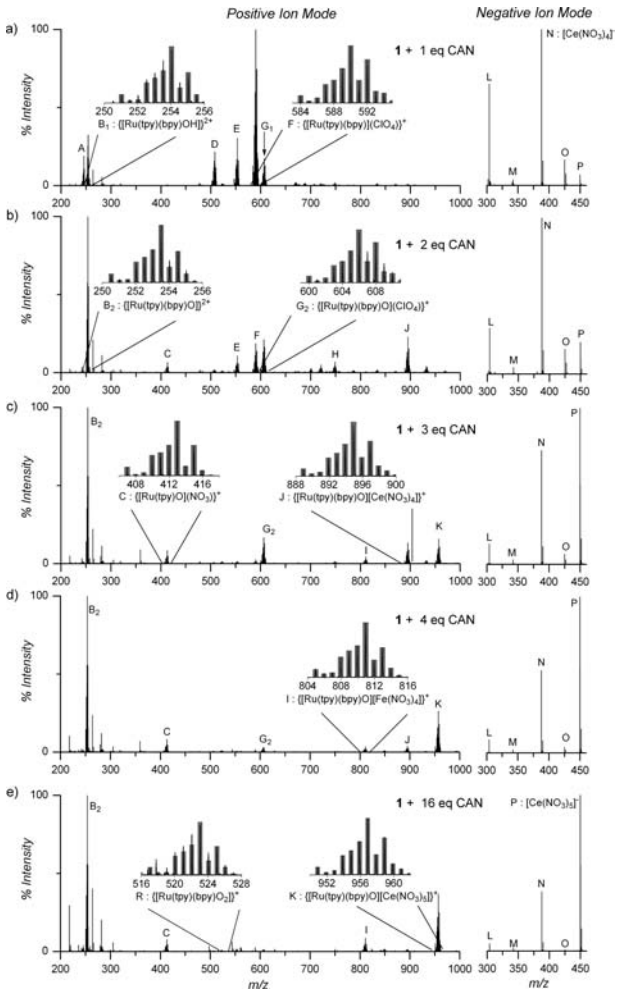

Figure 8. Positive and negative ion electrospray mass spectrum of a solution of **1** recorded immediately after the addition of (a) 1, (b) 2, (c) 3, (d) 4, and (e) 16 equiv (i.e., catalytic conditions) of CAN in 0.1 M HNO_3. *Insets*: Expanded *m*/*z* regions showing experimental and calculated isotope patterns of selected signals. Assignment of signals not described in figure: $[Ru(tpy)(bpy)]^{2+}$ (**A**); $[Ru(tpy)(bpy)OH]^{+}$ (**D**); $\{[Ru(tpy)(bpy)](NO_3)\}^{+}$ (**E**); $\{[Ru(tpy)(bpy)OH](ClO_4)\}^{+}$ ($\mathbf{G_1}$); $\{[Ru(tpy)(bpy)O][Fe(NO_3)_3]\}^{+}$ (**H**); $[Fe(NO_3)_4]^{-}$ (**L**); $[Ce(NO_3)_3O]^{-}$ (**M**); and $[Ce(NO_3)_3(ClO_4)]^{-}$ (**O**). The presence of $[Fe(NO_3)_4]^{+}$ is ascribed to slight dissolution of the steel tubing during these experiments.

signals of chemically similar compounds (e.g., $[Ru^{IV}{=}O]^{2+}$ versus $[Ru^{IV}{-}OO]^{2+}$).

Figure 8 shows the mass spectra of **1** measured shortly (t = 6 s) after the addition of 1, 2, 3, 4, and 16 equiv of CAN in 0.1 M HNO_3. The addition of 1−2 equiv of CAN (Figure 8a−b) reveals a solution with a mixture of the expected cationic Ru(III) and Ru(IV) metal species that reach a charge balance with the various anions present in solution (residual Ru(II) remains in solution due to slow reaction times or incomplete mixing). The spectrum obtained after the addition of 3 equiv of CAN to **1** does not reveal any signals corresponding to a $[Ru^{V}{=}O]^{3+}$ species in experiments recorded 6 s, 1 min (Figure 8c), 60 min, and 2 d after mixing the reagents. The addition of another equivalent of CAN (Figure 8d) leads only to a minor change in speciation. An interesting feature in both spectra is the over-representation of the complex ion pair $\{[Ru(tpy)(bpy)O][Ce(NO_3)_5]\}^{+}$ (**K**). Because ClO_4^{-}, NO_3^{-}, and $[Ce(NO_3)_4]^{-}$ are present in greater quantities than $[Ce(NO_3)_5]^{-}$ at this stage of the reaction, we view this as an indication that the $[Ru^{IV}{=}O]^{2+}$ fragment may have a higher affinity for $[Ce(NO_3)_5]^{-}$ than any

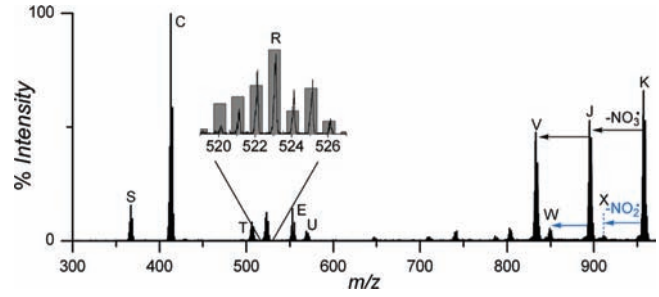

Figure 9. Positive ion ESI-MS/MS of $\{[Ru^{IV}(tpy)(bpy)O][Ce^{IV}(NO_3)_5]\}^{+}$ (**K**) in Figure 8 highlighting that $[Ru(tpy)(bpy)O_2]^{+}$ (**R**) is a product of the gas-phase fragmentation process. Remaining species are assigned as $[Ru(tpy)O]^{+}$ (**S**); $[Ru(tpy)(N_2C_{10}H_7)O]^{+}$ (**T**); $\{[Ru(tpy)(bpy)O](NO_3)\}^{+}$ (**U**); $\{[Ru(tpy)(bpy)O][Ce(NO_3)_3]\}^{+}$ (**V**); $\{[Ru(tpy)(bpy)O_2][Ce(NO_3)_3]\}^{+}$ (**W**); and $\{[Ru(tpy)(bpy)O_2][Ce(NO_3)_4]\}^{+}$ (**X**).

of the other anions present in solution. This observation provided a hint that perhaps an auxiliary reaction pathway involving $[Ce(NO_3)_5]^{-}$ was operative, where the Ce(IV) ion plays a role in activating one of the N−O bonds of the NO_3^{-}. It is also this special interaction that we hold responsible for the higher rates of electron transfer between the catalyst and CAN and/or the stabilization of the highly oxidizing $[Ru^{V}{=}O]^{3+}$/$[Ru^{IV}{=}O]^{2+}$ centers.

The mass spectrum recorded under catalytic conditions (i.e, **1**/CAN 1:16; $t \approx 10$ min after mixing; Figure 8e) provides a snapshot of the various intermediates that are generated in a genuine catalytic water oxidation reaction. ESI-MS has been used to characterize species at the end of a catalytic run,[32] but we are not aware of any other water oxidation catalyst that has been studied *in situ* with this particular technique. The spectrum under these conditions bears a close resemblance to those recorded after the addition of 3−4 equiv of CAN; however, there are new signals that are instructive to this analysis. For instance, we observe a signal corresponding to the dioxygen complex, $[Ru(tpy)(bpy)O_2]^{+}$ (**R**), which liberates dioxygen under MS/MS conditions (Figures 9 and S14). The intensity of **R** is only ∼1% of the mass spectrum, but it does provide rare *structural* evidence of an intermediate that occurs late in the catalytic cycle depicted in Figure 2. We rationalize this signal to be a consequence of a direct O−O interaction between the respective [Ru=O] and $[Ce(NO_3)]$ constituents. Similar experiments were conducted on **2**, and the solution-phase ESI-MS and MS/MS of the bimetallic $\{[Ru(tpy)(bpy\text{-}OMe)(O)][Ce(NO_3)_5]\}^{+}$ are shown in the Supporting Information (Figures S15 and S16). We note that dioxygen complexes of Ru and Ir have been previously observed by ESI-MS in gas phase reactions,[65,66] but the observation of such a species from a solution phase reaction has limited precedent.

$^{18}OH_2$-Labeling Studies. Compelling evidence that there are competing pathways to the acid−base pathway is provided by isotopic labeling experiments in $^{18}OH_2$-labeled water (Table 5). Tracking the relative concentrations of the gases that form in the headspace under catalytic conditions at pH 1 revealed that **1** and **2** produced a higher level of $^{16}O{=}^{16}O$ and lower levels of $^{16}O{=}^{18}O$ and $^{18}O{=}^{18}O$ than would otherwise be expected if only the acid−base mechanism is operative (reliable data for **3** could not be collected because of the formation of the

(65) Molina-Svendsen, H.; Bojesen, G.; McKenzie, C. J. *Inorg. Chem.* **1998**, *37*, 1981–1983.
(66) Thewissen, S.; Plattner, D.; Debruin, B. *Int. J. Mass Spectrom.* **2006**, *249−250*, 446–450.

Table 5. Relative Abundance of $^{16}O{=}^{16}O$, $^{16}O{=}^{18}O$, and $^{18}O{=}^{18}O$ Generated during the Oxidation of $^{18}OH_2$-Labeled Water by **1** and **2** in 0.1 M HNO_3[a]

		relative abundance		
		observed[b]	theoretical[c]	% deviation[d]
1	$^{16}O{=}^{16}O$	0.90(3)	0.837	8
	$^{16}O{=}^{18}O$	0.09(3)	0.156	−41
	$^{18}O{=}^{18}O$	0.004(1)	0.0072	−45
2	$^{16}O{=}^{16}O$	0.862(1)	0.843	2
	$^{16}O{=}^{18}O$	0.133(1)	0.150	−11
	$^{18}O{=}^{18}O$	0.055(1)	0.0067	−18

[a] [Ru] = (2.9−3.4) × 10^{-4} M; [CAN] = 0.08−0.09 M; total volume = 2.9−3.5 mL. [b] Relative ratios of dioxygen signals; standard deviations of no less than three trials are indicated in parentheses. [c] Probability of 10% $^{18}OH_2$-labeled water producing $^{32}O_2$, $^{34}O_2$, and $^{36}O_2$ is 0.81, 0.18, and 0.01, respectively; values in table account for dilution factors. [d] % deviation = (observed − theoretical)/theoretical ×100%; theoretical values assume both O-atoms of dioxygen are derived from water.

precipitate). Given that the only other source of oxygen present in the respective reaction flasks is a stoichiometric quantity of ClO_4^- counterions and a significant excess of NO_3^- (from the acid and CAN), we infer that the anions are involved in the O−O bond-forming step. (Note that control experiments exclude ^{18}O being incorporated into CAN on a relevant time scale and the possibility that the O-atoms of bpy-OMe are introduced into the dioxygen product during the analysis of **2**.) It is primarily on these grounds that we invoke the OAT pathway k_{OAT} in Figure 2. The results in Table 5 support the notion that an O-atom is derived from a species other than water. In the case of **2**, for example, the isotopic distribution is consistent with 10−12% of the evolved dioxygen containing an O-atom from CAN (or another source other than water) via an OAT pathway. (Note that the relative ratios of isotopomers preclude atmospheric dioxygen being a source of the large % deviations in Table 5.)

In order to corroborate our theory of a reaction step involving OAT, we set out to verify the exclusion of NO_2 during catalysis (see k_{OAT} in Figure 2). While GC-MS did not prove to be an effective method for detecting this particular species at modest concentrations, we found laser cavity ring-down spectroscopy to be a useful tool in this regard: NO_2 was detected immediately following the addition of catalyst to a solution of CAN in 1.0 M HNO_3 (Figure S17). Moreover, the maximum rate of NO_2 evolution tracks the maximum rate of dioxygen evolution (a short delay in signal response is due to transit of the analyte to the sensor within the sample chamber). In combination with the $^{18}OH_2$ labeling studies, the detection of NO_2 provides strong evidence of the existence of the O-atom transfer pathway defined in Figure 2.

Discussion

This study builds on the mechanistic studies of homogeneous water oxidation catalysts that have recently appeared in the literature by establishing specifically how electron density at the metal site affects the catalytic activity of mononuclear octahedral polypyridyl Ru(II) complexes related to **1**. Our mechanistic studies, augmented by the use of ESI-MS as a probe under catalytically relevant conditions, unveils a complicated reaction landscape that expands on the prevailing acid−base mechanism documented by Meyer et al.[31] A full description of the mechanistic details for **1**−**3** is addressed in sequence below.

Description of Catalytic Cycle for 1. Our data indicate that the catalytically active forms of the Ru catalysts in this investigation are the aqua-derived species, [Ru−OH_x]. Previous findings by Sakai and our program show that a Ru−Cl bond is not required for catalysis and the presence of coordinating ligands (e.g., MeCN, Cl^-, SO_4^{2-}) actually suppresses catalytic activity.[33,48] Thus, the starting point in the proposed catalytic cycles for **1**−**3** is the $[Ru^{II}{-}OH_2]^{2+}$ form of the catalyst. Our spectrophotometric determination of relevant pK_a values and Pourbaix diagrams indicate that the first oxidation of **1** by CAN is an electron-transfer process in a strongly acidic medium, while the second oxidation process is accompanied by the loss of two protons to generate $[Ru^{IV}{=}O]^{2+}$ in solution. At higher pH levels, these two steps would formally be consecutive PCET processes. This scenario differs slightly from that of **IV**[31] because of the higher relative stability of the Ru(III) redox level for **1**.

The assignment of the latter stages of the catalytic cycle becomes significantly more arduous, particularly because reaction conditions play a critical role in the reactivity. For example, even when all other experimental parameters are held at parity, k_{cat} values are measured in the presence of 30 equiv of CAN, while k_1−k_3 and k_{O-O} are measured in the presence of 1−3 equiv of CAN. These disparate conditions appear to evince different reaction pathways. Evidence to support this includes the fact that the reaction of 1 equiv of CAN with $[Ru^{IV}{=}O]^{2+}$ does not produce spectroscopically distinct trends that correspond to the successive formation of $[Ru^{V}{=}O]^{3+}$ and $[Ru^{III}{-}OOH]^{2+}$, yet dioxygen evolution is observed with a k_{cat} value of 6.6 × 10^{-4} s^{-1} under catalytic conditions. We therefore contend that, at a **1**/CAN ratio of 1:1, the electron-transfer reaction between $[Ru^{IV}{=}O]^{2+}$ and CAN does not occur (the oxidation of $[Ru^{IV}{=}O]^{2+}$ by CAN is a formally endothermic process; ΔG = +32 kJ/mol) or is slower than k_{O-O}; it is difficult to resolve these two possibilities spectrophotometrically. Reaction step k_d may also be responsible for the slow decay in the titration experiments but is expected to be too slow to be relevant under catalytic conditions.

Under conditions of excess CAN, the acid−base reaction steps all become accessible due to equilibrium considerations (including the Nernstian effect on the Ce(IV)/Ce(III) potential) to ultimately form $[Ru^{IV}{-}OO]^{2+}$, which precedes the RDS, k_{O2} (in 0.1 M HNO_3). Tracking the catalytic mixture (i.e., **1**/CAN 1:30) converges on a spectral signature consistent with a Ru(IV) species (Figure 6a). These data suggest that $[Ru^{IV}{=}O]^{2+}$ and/or $[Ru^{IV}{-}OO]^{2+}$ are the dominant forms of the catalyst under catalytic conditions, which would be expected given the demands associated with the oxidation of $[Ru^{IV}{=}O]^{2+}$ and the exclusion of dioxygen from a Ru(IV) center. The spectrophotometric determination of k_{cat} following the addition of 30 equiv of CAN to **1** also follows the expression $rate = k_{cat}[\mathbf{1}]$ to support k_{O2} being the RDS.

A characterization of the products that form in the headspace of the reaction flask under catalytic conditions reveals a ratio that is not in full agreement with both O-atoms in dioxygen being derived from water. Indeed, the isotopic distribution of $^{16}O{=}^{16}O$, $^{16}O{=}^{18}O$, $^{18}O{=}^{18}O$ in the headspace of the reaction flask is consistent with a competing reaction pathway involving the abstraction of an O-atom from a NO_3^- anion by the catalyst. The detection of NO_2 by laser cavity ring-down spectroscopy further corroborates the k_{OAT} pathway described in Figure 1. Chemical insight into this auxiliary pathway is provided by the ESI mass spectrum of **1** recorded under catalytic conditions, which reveal a prominent signal corresponding to the complex ion, $\{[Ru(tpy)(bpy)O][Ce(NO_3)_5]\}^+$. The intensity of this signal, despite the prevalence of other anions in solution, hints at an affinity between $[Ru^{IV}{=}O]^{2+}$ and the Ce(IV) salt; this statement

is bolstered by titration experiments. Further support for an interaction between the $[Ru{=}O]^{2+}$ unit and $[Ce(NO_3)_5]^-$ is that fragmentation of $\{[Ru(tpy)(bpy)O][Ce(NO_3)_5]\}^+$ by MS/MS results in the dioxygen species, $[Ru^{III}{-}OO]^+$. Our interpretation of this entire collection of data is that the Ce(IV) ion plays a role in activating a N−O bond of a NO_3^-; i.e., the O-atom is not derived from a free NO_3^- ion. This is supported by myriad control experiments and isotopic labeling experiments indicating a suppression of the OAT pathway in other acids (e.g., triflic acid).

Description of Catalytic Cycle for 2. The first two oxidation processes for **2** are rapid and furnish the $[Ru^{IV}{=}O]^{2+}$ species. The third oxidation process is assigned as the generation of the ostensible $[Ru^{V}{=}O]^{3+}$ species, which is then poised for nucleophilic attack by an incoming water substrate. The rate of this latter reaction was determined by the onset of a signal at 320 nm shortly after the addition of 1 equiv of CAN to $[Ru^{IV}{=}O]^{2+}$ ($k_{O-O} = 3.3 \times 10^{-5}$ s^{-1}). The lower magnitude of k_{O-O} relative to **IV** ($k_{O-O} = 9.6 \times 10^{-3}$ s^{-1}) is aligned with a lower electrophilicity of the [Ru=O] fragment due to the electron-donating groups, but we caution that competing pathways in solution may falsely represent the k_{O-O} value. In the case of **IV**, the $[Ru^{III}{-}OOH]^{2+}$ is found to disproportionate to $[Ru^{II}{-}H_2O_2]^{2+}$ and $[Ru^{IV}{-}OO]^{2+}$ due to the instability of the Ru(III) level. This decay is not observed for **2** because of the stabilization of the Ru(III) level by the electron-rich −OMe groups.

The observation of k_3 for **2**, but neither **1** nor **3**, is rationalized in part by the lower thermodynamic demands associated with oxidizing the $[Ru^{IV}{=}O]^{2+}$ form of **2**. Because the same is true for k_5, this oxidation step late in the catalytic cycle becomes accessible for **2**; this step becomes rate-determining and follows the rate expression $rate = k_{cat}$[**2**][CAN] (where $k_{cat} = 1.0$ M^{-1} s^{-1}). The faster k_{cat} value for **2** relative to **1** and **3** indicates that the exclusion of dioxygen from a Ru(V) species is faster than that from a Ru(IV) level; the difference may also be ascribed to EDGs enhancing cleavage of the peroxo ligand from the Ru complex.[37] The time-dependent spectra recorded for **2** following the addition of 30 equiv of CAN collapse to an absorption envelope that does not match exactly the $[Ru^{IV}{=}O]^{2+}$ species but does bear features that would be expected for either $[Ru^{V}{=}O]^{3+}$ or $[Ru^{IV}{-}OO]^{2+}$. This provides further evidence that significant reaction barriers in the catalytic cycle involve dioxygen formation and access to the Ru(V) level. The lower TONs observed for **2** relative to the other catalysts when a large excess of CAN is used can be rationalized by the buildup of the Ru(V) level preceding the slow k_{O-O} step; i.e., the $Ru{-}N_{bpy}$ bond trans to the oxo ligand is susceptible to cleavage, and increasingly so at higher redox levels, such that catalyst degradation is faster for **2**.[48] On these same grounds, the $[Ru^{IV}{-}OO]^{2+}$ form of **2** may also be a point of departure in the catalytic cycle.

Taking into account that the purported k_{O-O} step is slower relative to k_{cat}, we suggest that **2** partially bypasses the acid−base mechanism under catalytic conditions to proceed through an OAT process with CAN via k_{OAT}. This hypothesis is rationalized by the fact that the Ru(V) redox level is more accessible to electron transfer with CAN, but the $[Ru^{V}{=}O]^{3+}$ fragment may not be sufficiently susceptible to nucleophilic attack by water because of the electron-donating substituents. Offering support for this hypothesis is the relative ratios of the isotopically labeled dioxygen species formed in the reaction (Table 5), which shows clear evidence that an O-atom is derived from a source other than water under catalytic conditions, the evolution of NO_2 during catalysis, and the greater than stoichiometric amounts of dioxygen formed during the reaction (Table 4). This same alternative pathway is available for both **1** and **3**, but may be less likely to occur because k_{O-O} is presumably faster for these two catalysts relative to **2** due to the electrophilicity of the $[Ru^{V}{=}O]^{3+}$ fragment.

Description of Catalytic Cycle for 3. The first two (proton-coupled) electron-transfer steps were found to be the fastest for **3** among the series, an observation that is attributed to a combination of thermodynamic driving force and the electrostatic interaction between the cationic $[Ru{-}OH_n]^z$ unit and $[Ce^{IV}(NO_3)_5]^-$. These well-defined steps are followed by the reactivity of the $[Ru^{IV}{=}O]^{2+}$ form that is not entirely consistent with the behavior of **1** or **2**. The $[Ru^{IV}{=}O]^{2+}$ form not only spontaneously decays in solution to a $[Ru^{III}{-}OH]^{2+}$ species due to an apparent disproportionation pathway, but spectral features arise that are consistent with the formation of $[Ru^{II}{-}O_2H_2]^{2+}$ via k_{O-O}'. We believe this is the first evidence of O−O bond formation at a Ru(IV) site for any single-site catalyst. We ascribe the formation of a $[Ru^{III}{-}OH]^{2+}$ species to a slow k_d step; the concomitant formation of $[Ru^{V}{=}O]^{3+}$ is followed by a rapid k_{O-O} step to form $[Ru^{III}{-}OOH]^{2+}$. The observation of dioxygen formation in electrochemical experiments where the potential is held at 1.7 V (i.e., below the Ru(V)/Ru(IV) potential) lends further support to at least one of these pathways occurring in solution.

Tracking the spectral changes at 322 nm following the addition of 1 equiv of CAN to the $[Ru^{IV}{=}O]^{2+}$ form of **3** reveals the onset of one species at a rate of ∼2 M^{-1} s^{-1}, followed by the formation of a second species at a rate of 1×10^{-4} s^{-1}; these trends are consistent with successive k_d and k_{O-O} steps.[67] A separate process is also occurring that is consistent with the formation of a $[Ru^{II}{-}O_2H_2]^{2+}$ complex (k_{O-O}') based on the onset of a shoulder at 483 nm, followed by the formation of $[Ru^{III}{-}OOH]^{2+}$ (k_3'). We do not rule out the possibility of a slow k_d process and comparable k_{O-O} step, followed by a rapid k_4 step leading to $[Ru^{IV}{-}OO]^{2+}$, which would be in resonance with a Ru(II) dioxygen complex (eq 12). This latter species would be stabilized by the electron-withdrawing groups and is consistent with the feature at 486 nm.

Under catalytic conditions (i.e., 30 equiv of CAN), **3** is found to follow the same rate expression as that for **1**. Because k_{O-O} is presumably faster for **3** than **1**, the RDS is assigned as k_{O2}. Under steady-state conditions, the emergence of a signal at 486 nm is observed, which we assign as the stabilization of the Ru(II) resonance form in eq 12. Computational studies are underway to unravel the nature of this interaction for the series.

Interaction of CAN with the Catalyst. This study raises the issue that the interaction between the catalyst and CAN may need to be given consideration in studies of this type. Making it somewhat difficult to pinpoint this behavior is the fact that the nature of CAN in solution has not been unambiguously defined in the literature. Based on our ESI-MS experiments, CAN appears to exist predominantly as $[Ce(NO_3)_5]^-$ in a HNO_3 medium (Figure S18). Noting that CAN exists as $[Ce(NO_3)_6]^{2-}$ in the solid state,[68] this dianionic form does not appear to be the dominant species in solution (we do not rule out the possibility that $[Ce(NO_3)_6]^{2-}$ is the dominant species in solution and undergoes charge reduction in the spectrometer). There is

(67) These data assume appropriate second-and first-order kinetics.
(68) Dvorkin, A. A.; Krasnova, N. F.; Simonov, Y. A.; Abashkin, V. M.; Yakshin, V. V.; Malinovskii, T. I. *Kristallografiya* **1984**, *29*, 471.

also evidence for $[Ce(NO_3)O]^-$ in solution (that presumably exists as $[Ce(NO_3)_3(OH)]$ prior to charge reduction in the MS instrument), which is more prevalent at higher pH values, our interpretation of the data in acidic media only considers the interaction of the catalyst with $[Ce(NO_3)_5]^-$. The anionic nature of this ion presumably helps to facilitate intermolecular interactions with the positively charged catalysts in the various valent forms. Isotopic labeling experiments show that O-atom exchange with NO_3^- in the absence of CAN with or without the catalyst at 0.1 and 1.0 M HNO_3 does not occur on a relevant time scale to influence the data presented in Table 5.

Our experiments show that the NO_3^- anions affect the reactivity of these catalysts in two ways: (i) they can oxidize Ru(II) to Ru(III) in strongly acidic media (eqs 2−4), and (ii) they can be a source of oxygen in the critical O−O bond-forming step by way of a reaction with the high-valent [Ru═O] unit. Because control experiments rule out dioxygen formation between the Ru complexes and free NO_3^- anions, and because the amount of dioxygen produced in the case of **2** testifies to NO_3^- being at least one source of extrinsic oxygen, we believe the high positive charge of the Ce(IV) ion, in tandem with the high valent [Ru═O] unit, is critical to activating an N−O bond of the NO_3^- anion. Our kinetic studies do not show clear evidence for the $[Ru^{IV}═O]^{2+}$ forms of **1** nor **2** being sufficiently electrophilic to abstract an O-atom from $[Ce^{IV}(NO_3)_5]^-$ (or $[Ce^{III}(NO_3)_4]^-$) in solution. On this basis, we propose that it is the $[Ru^{V}═O]^{3+}$ form of the catalyst that abstracts an O-atom from $[Ce(NO_3)_5]^-$ (i.e., k_{OAT} in Figure 2). This proposal invokes the production of $[Ce^{IV}(NO_3)_4]$, which presumably is regenerated to $[Ce^{IV}(NO_3)_5]^-$ in the acid medium to enable subsequent electron-transfer processes and can therefore render catalytic efficiencies in excess of 100%. The possibility that k_{OAT} involves ClO_4^- is not wholly dismissed, but we postulate that $[Ce^{IV}(NO_3)_5]^-$ is the predominantly reactive anion on the grounds that ClO_4^- is not present in sufficiently high concentrations and the relative pK_a values of HNO_3 and $HClO_4$. Further support is provided by ESI-MS studies, which show an apparent propensity of the high-valent [Ru═O] forms of either **1** and **2** to form ion pairs in solution with $[Ce(NO_3)_5]^-$, despite the much higher concentration of NO_3^-, and in certain cases $[Ce(NO_3)_4]^-$, in solution under catalytic conditions. The gas-phase fragmentation of this complex ion pair renders a [Ru−OO] complex, which lends some credence to there being a bonding interaction between the catalyst and Ce salt. A related set of catalytic experiments involving **1** in other acids (e.g., HOTf) indicates a suppression of the OAT pathway. This result is attributed to the displacement of the NO_3^- ligands about the Ce(IV) ion by the respective acid anion (e.g., OTf^-), which effectively inhibits an interaction between the activated $[Ce(NO_3)_5]^-$ complex and the [Ru═O] unit. These collective observations further underscore the importance of understanding the chemical behavior of the terminal oxidant when assessing the mechanistic behavior of water oxidation catalysts.

Conclusions

This study provides evidence that catalytic water oxidation driven by CAN provides access to reaction pathways that diverge from the prevailing "acid−base" mechanism for single-site catalysts. The preference for each of these pathways is dependent on reaction conditions and electron density at the metal site. The position of the RDS is shown to be sensitive to electron density at the Ru center and shows that higher catalytic activity is attained when the $[Ru^{V}−OO]^{2+}$ is made accessible (i.e., RDS is k_{O2}' rather than k_{O2}). However, too much density at the metal site can compromise the critical bond formation step, thus highlighting the inherent limitation for achieving high catalytic rates with catalysts of this type. This study also demonstrates that a minor auxiliary reaction pathway may be operative that enables the incorporation of an O-atom from a source other than water (e.g., CAN) into the dioxygen product. These findings provide important insight into the design and study of homogeneous water oxidation catalysts.

Acknowledgment. The authors thank Dr. Scott McIndoe (University of Victoria) for access to ESI-MS instrumentation. This work was financially supported by the Canadian Natural Science and Engineering Research Council (NSERC), Canada Research Chairs, Canada Foundation for Innovation, and Alberta Ingenuity.

Supporting Information Available: Experimental details, dioxygen and NO_2 evolution traces, and spectrophotometric and electrochemical data. This material is available free of charge via the Internet at http://pubs.acs.org.

JA106108Y